

FERMIONIC STATE PREPARATION AND IMAGING IN OPTICAL TWEEZER ARRAY

Khoruzhii Kirill
Munich, May 19, 2025

Quantum simulation with ultracold atoms requires both high-fidelity preparation of the initial many-body state and site-resolved measurement of the final state. This thesis presents the development of experimental techniques for spin-resolved free-space imaging and deterministic, spin-selective preparation of ultracold fermionic ${}^6\text{Li}$ atoms in a two-dimensional optical tweezer array. The array is generated using crossed acousto-optic deflectors, with precise control achieved through a combination of direct camera-based calibration and atom-based feedback. A novel spilling method enables the preparation of arbitrary spin- and site-resolved occupation patterns. The thesis also introduces numerical tools for simulating Fermi-Hubbard dynamics in small systems, laying the groundwork for future out-of-equilibrium quantum simulation experiments.

Contents

1	Introduction	10
1.1	Quantum Simulation with Fermionic Tweezer Arrays	10
1.2	Thesis Outline	10
2	Single-atom spin-resolved free-space imaging	11
2.1	Motivation and background	11
2.2	Experimental setup	11
2.3	Image processing	11
2.4	Spin-resolved detection	11
3	Tweezer array system	12
3.1	Motivation and concept	12
3.2	Optical setup	13
3.3	State preparation	13
3.4	Control	14
3.5	Tweezer depth balancing	14
3.6	Spin-selective spilling	15
3.7	Arbitrary occupation loading	15
4	Matter-wave magnifier	17
4.1	Motivation and overview	17
4.2	Numerical modeling	17
5	Fermi-Hubbard model: numerical approaches and simulations	18
5.1	Motivation and experimental relevance	18
5.2	Theoretical and numerical methods	18
5.3	GPU-accelerated implementation	18
5.4	Simulations of noisy dynamics	18
6	Appendix	19
6.1	Boolean matrix factorization	19

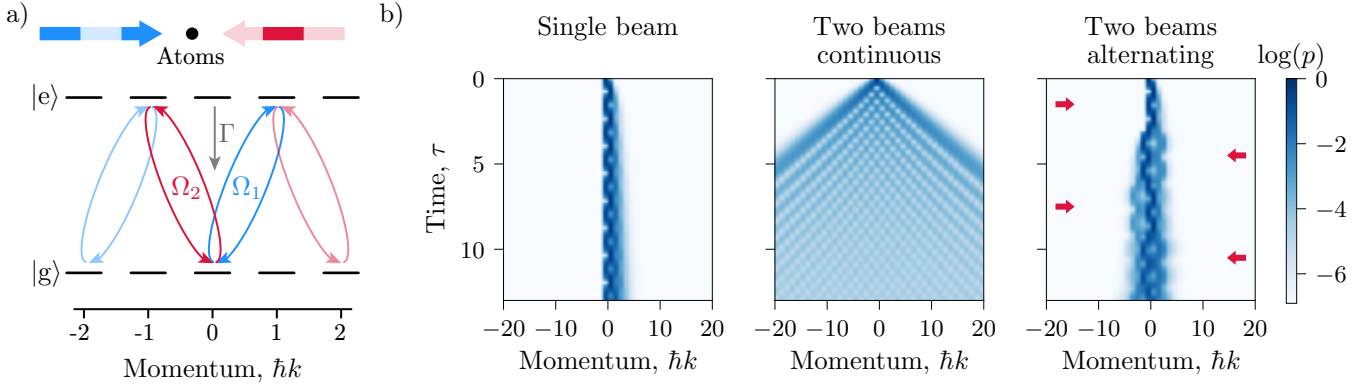


Figure 1: **Momentum-space dynamics in the SSH model.** a) Atoms undergo momentum-changing transitions via couplings Ω_1 and Ω_2 , realizing a SSH-like quantum walk. b) Momentum distributions over time for different beam configurations: single beam (left) shows small shift; two continuous beams (middle) result in fast spreading; alternating beams (right) suppress spread.

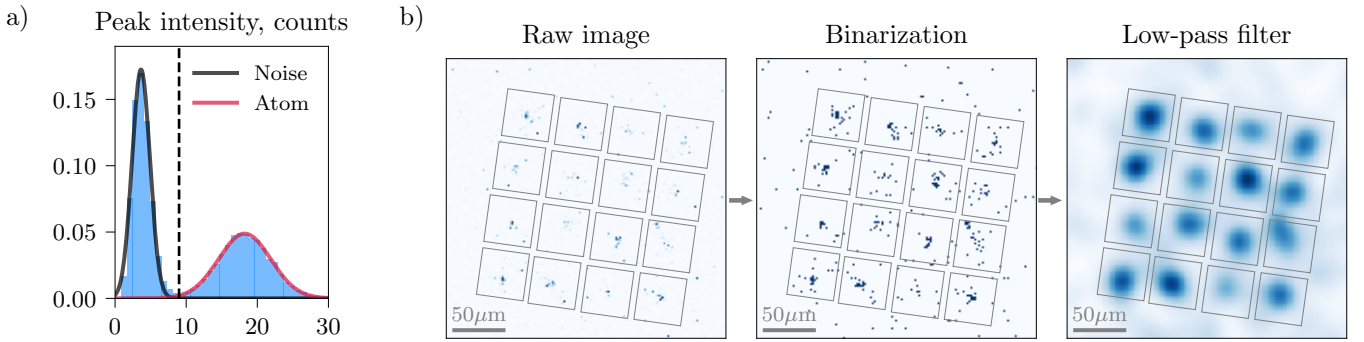


Figure 2: **Single-atom identification and image processing.** a) Histogram of peak intensities extracted from binarized and low-pass filtered images shows a bimodal distribution: the first peak corresponds to camera noise (black), the second corresponds to single atoms (red). The dashed line indicates the threshold used for atom identification. b) Image processing pipeline: Raw fluorescence image (left), binarization by intensity thresholding (center), and application of a low-pass filter (right) to reveal spatially localized atomic signals.

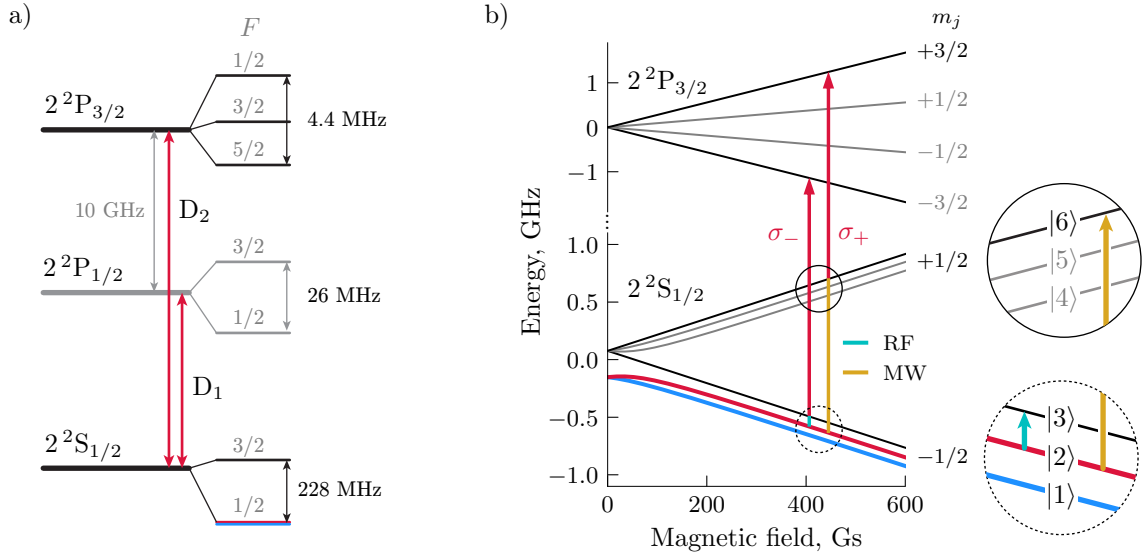


Figure 3: ${}^6\text{Li}$ energy levels. a) Level diagram of the ground and excited states of ${}^6\text{Li}$ [6], including the D₁ and D₂ transitions around $\lambda = 671$ nm. b) Zeeman splitting of the hyperfine levels of the $2^2\text{S}_{1/2}$ and $2^2\text{P}_{2/2}$ in ${}^6\text{Li}$ [12, 16]. As different spin states for physics we consider state $|1\rangle$ and $|2\rangle$, but for imaging it is worth to flip them to stretched states $|6\rangle$, $|3\rangle$. Colored lines indicate transitions driven by radiofrequency (RF) and microwave (MW) fields.

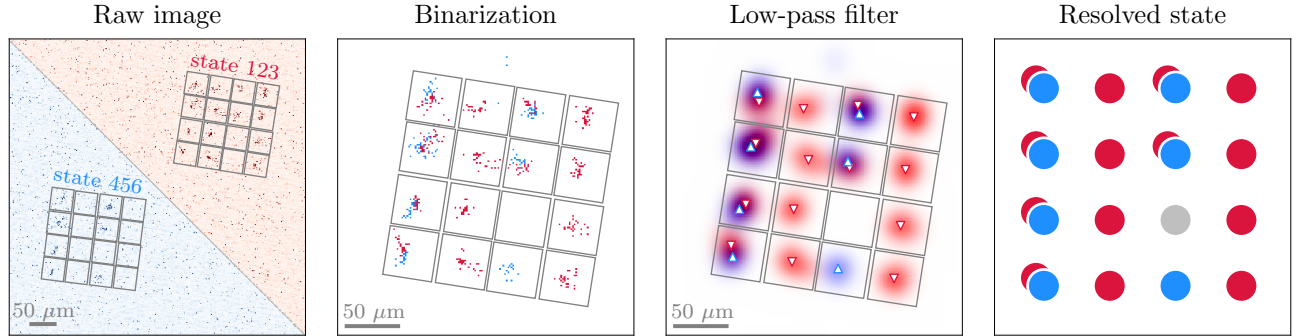


Figure 4: Spin-resolved single-atom imaging. Spatially separated σ_+ and σ_- fluorescence is imaged onto two distinct regions of the camera. The binarization step identifies photon counts above a threshold, followed by a low-pass filter to extract spatially localized signals. Final spin states are assigned based on relative signal strength in each channel: ● – $|1\rangle$, ● – $|2\rangle$, ● – no atom.

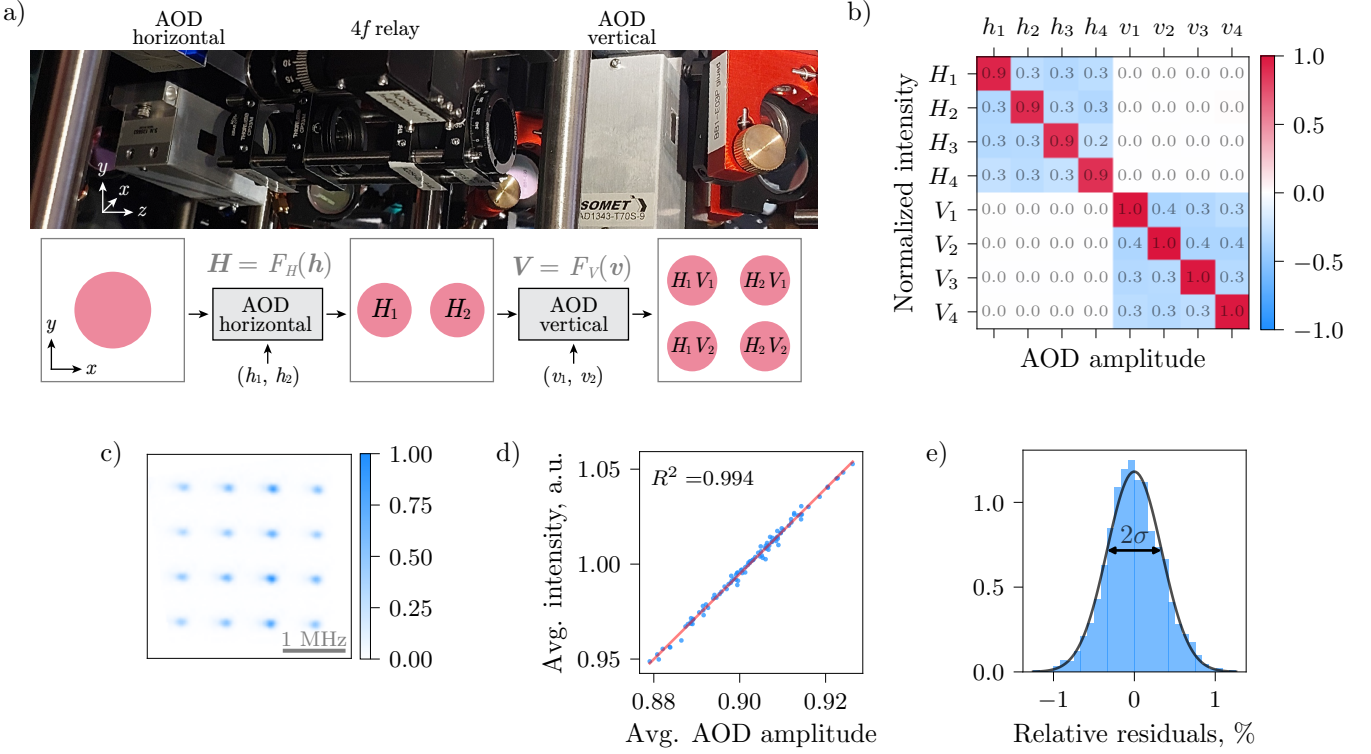


Figure 5: **Tweezer array control using orthogonal AODs.** (a) Experimental setup: two orthogonal AODs generate a 2D tweezer array. The applied harmonic amplitudes h_i , v_j define the output intensities $H_i = F_H(h)$ and $V_j = F_V(v)$ in horizontal and vertical directions, respectively. (b) Crosstalk matrix F' reconstructed via linear regression from camera images, showing how modulation of one harmonic affects others. (c) Example of measured intensity distribution at uniform input amplitudes ($h_i = v_j = 0.9$), illustrating imbalance in the resulting pattern. (d) The total intensity $\Lambda = \sum_{ij} H_i V_j$ scales linearly with the mean input amplitude. (e) Residuals of the linear model (fitted in the range [0.85, 0.95]) are normally distributed. All data were obtained in this work using direct camera-based measurements.

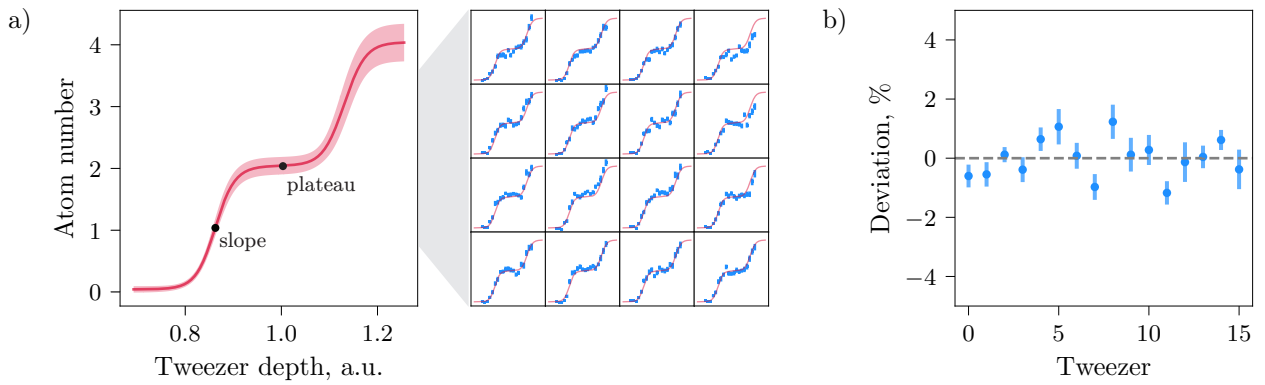


Figure 6: **Step plot.** (a) Atom number as a function of tweezer depth during the spilling sequence. Step plots for each tweezer in the 4×4 array are shown on the right. The average fit is shown as a solid red line, with standard deviation across sites indicated by the shaded area. (b) Relative deviation of the fitted sigmoid centers for each tweezer after SVF balancing. The standard deviation is $0.7(2)\%$, which is well within the plateau width ($\pm 5\%$), ensuring sufficient uniformity for array-wide spilling. $\chi^2?$

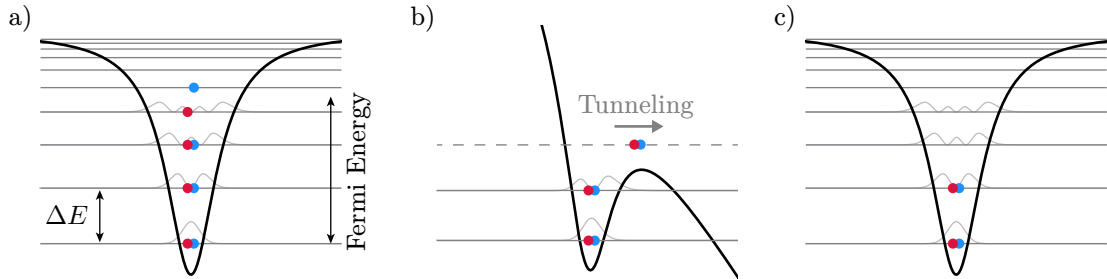


Figure 7: **Deterministic preparation via spilling.** (a) Fermionic atoms are initially loaded into a tightly confined optical tweezer, forming a Fermi sea occupying the approximately 1D harmonic oscillator levels up to the Fermi energy. (b) A magnetic field gradient tilts the potential, and the trap depth is lowered such that atoms above a defined spill level tunnel out. (c) This procedure leaves a well-defined number of atoms in the lowest energy states, with a preparation fidelity of approximately 95%. Blue and red dots denote atoms in different spin states; gray curves indicate the bound-state wavefunctions.

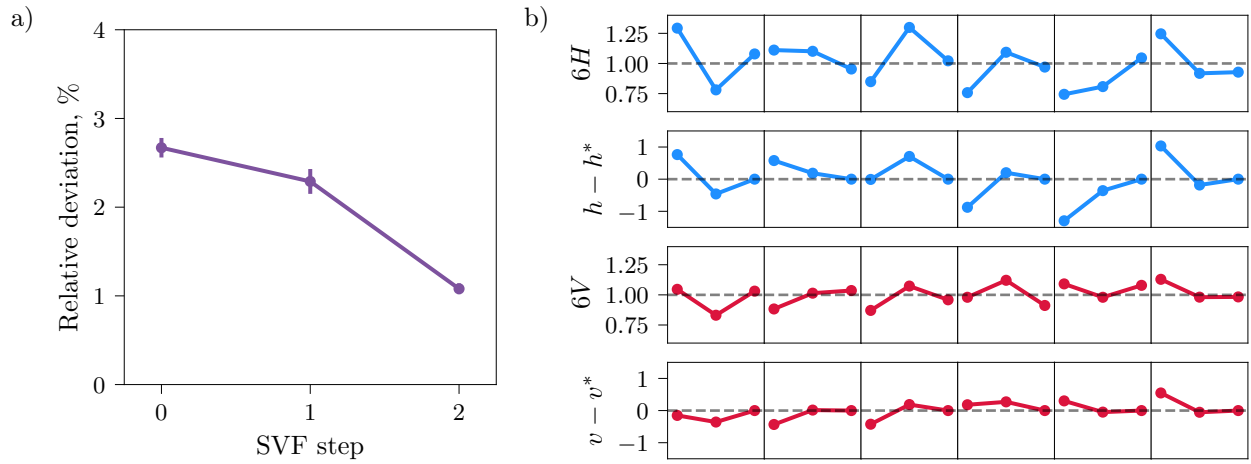


Figure 8: **Single-value feedback (SVF) optimization for a 6×6 tweezer array.** (a) Relative deviation of effective powers P_j across the array during successive SVF steps, quantified as $\text{std}(P_j)/\langle P_j \rangle$. The initial point corresponds to camera-based balancing; subsequent iterations apply SVF with feedback rates $\gamma = 1/20$ and $\gamma = 1/40$. Further iterations did not yield statistically significant improvements. (b) Retrieved horizontal powers H_i and vertical powers V_j (top and third rows), along with corresponding deviations of driving amplitudes from their final target values, $h - h^*$ and $v - v^*$. The recovered H , V vectors are extracted from the photon count matrix M_{ij} using factorization as described in (3).

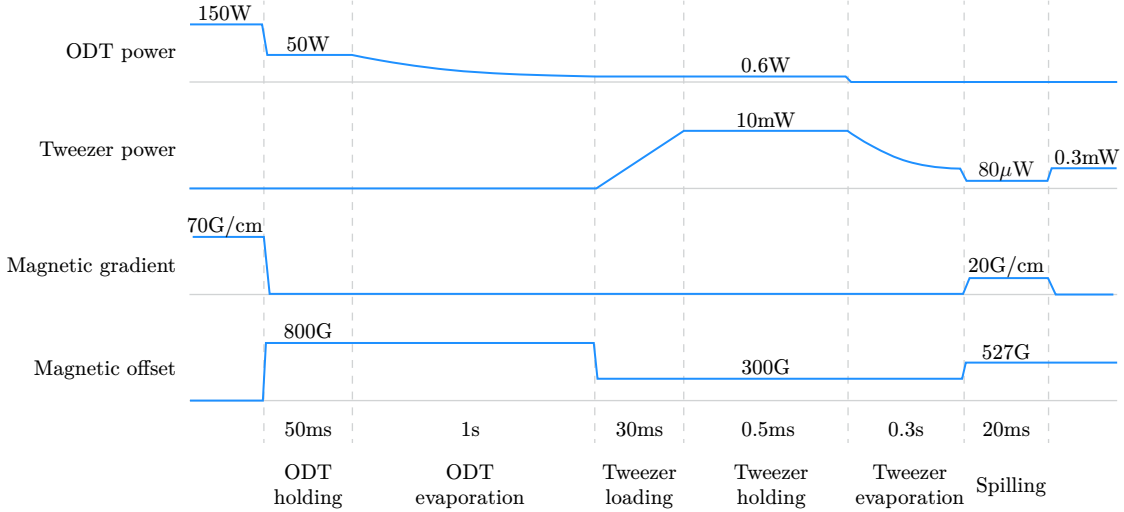


Figure 9: Experimental sequence for deterministic atom number preparation. After loading a spin-balanced mixture into a crossed ODT from the MOT, we perform two-stage evaporation in the ODT. The atoms are then transferred into an optical tweezer via an adiabatic ramp. Further evaporation is carried out in the tweezer before executing the spilling procedure. Spilling takes place at 527 G and a magnetic field gradient of 20 G/cm to remove atoms above the spill level. The full sequence enables high-fidelity few-body preparation within a sub-2 s cycle time. A detailed description can be found in [4].

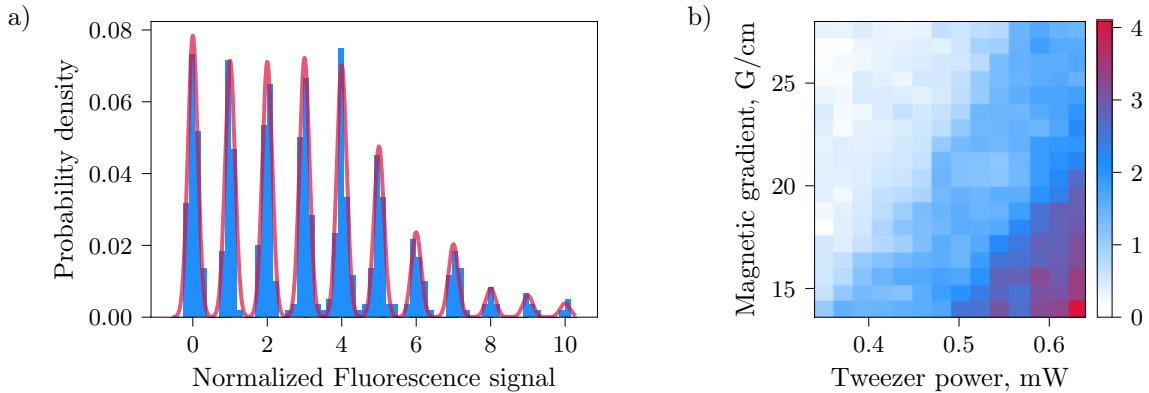


Figure 10: (a) Histogram of the normalized fluorescence signal after loading to the MOT, showing clear quantized peaks corresponding to integer atom numbers. The solid red line is a multi-Gaussian fit to the observed distribution. (b) Measured 2D step plot as a function of tweezer power and magnetic field gradient. Each point indicates the average atom number obtained for a given combination of parameters. This map confirms that for any spill power, a suitable magnetic gradient can be found to achieve a desired quantized atom number.

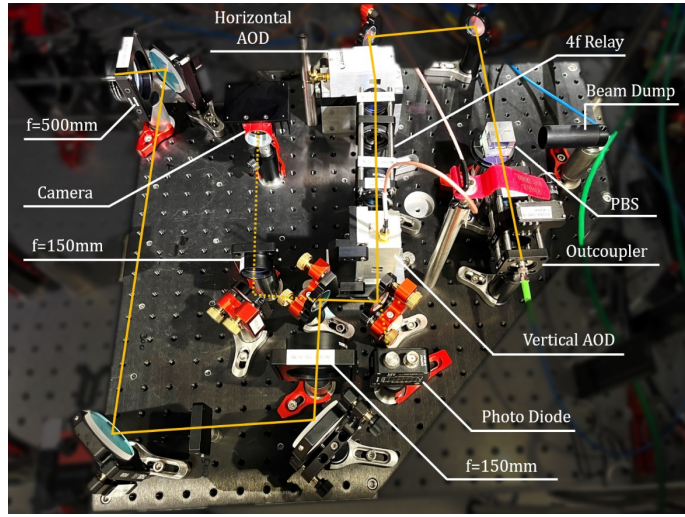


Figure 11: **Optical setup for 2D tweezer array.** The beam path (solid orange line) includes two orthogonal AODs, a $4f$ relay, and diagnostic components. Dashed lines indicate monitoring light paths. Taken from [4].

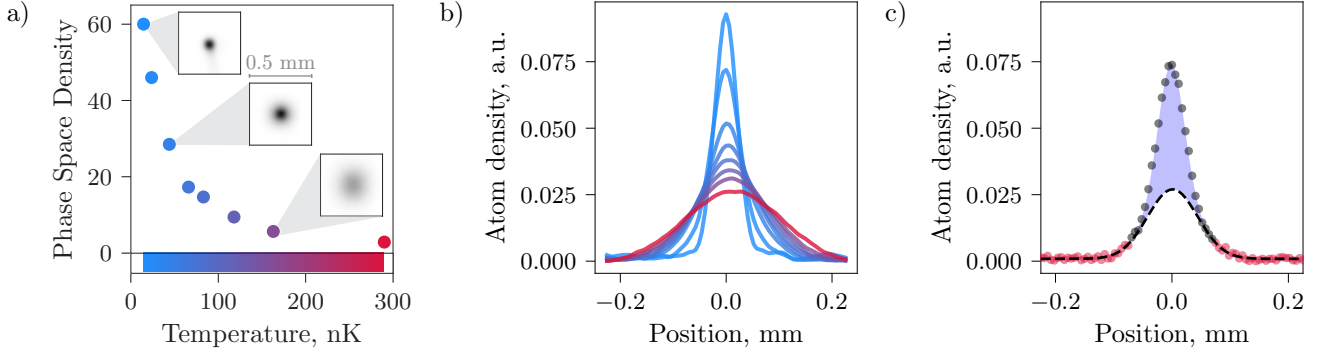


Figure 12: **Molecular Bose-Einstein condensate data.** (a) Phase space density (PSD) increases as temperature decreases via evaporative cooling, indicating condensation onset. (b) Atom density profiles normalized to unit area; color encodes temperature as in (a). (c) At low temperature, the profile shows a bimodal shape: a Gaussian fit to thermal wings (red dots) underestimates the central peak, revealing the mBEC component (blue area).

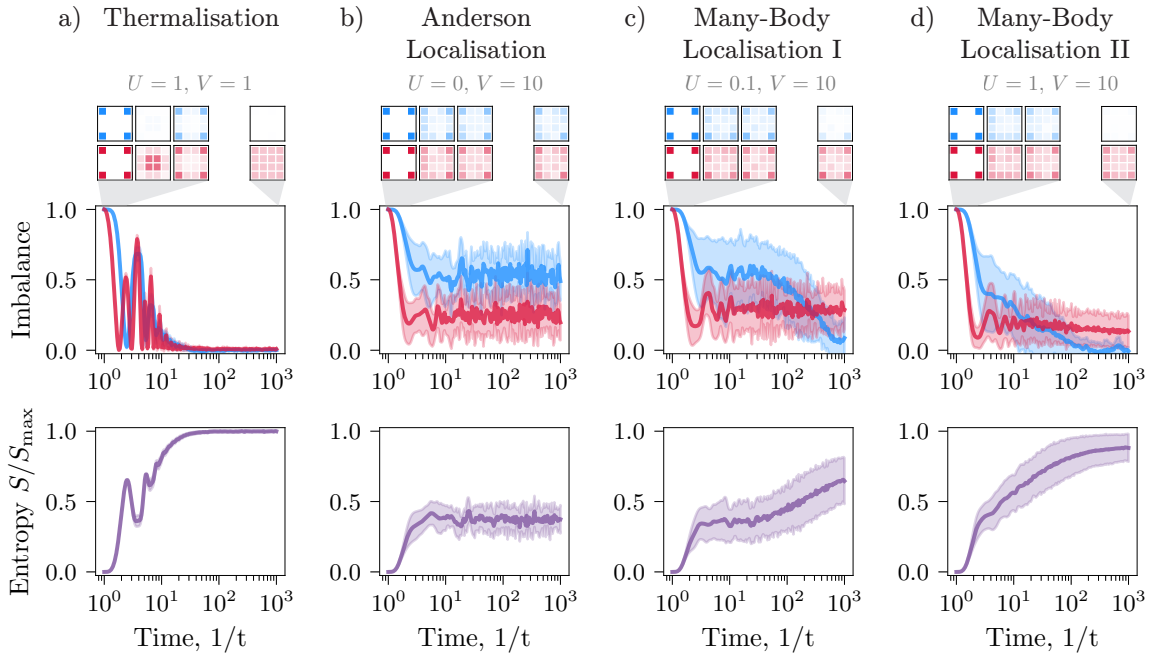


Figure 13: **Dynamical phases in a 2D Fermi-Hubbard system.** Top: Snapshots of particle density (red) and magnetization magnitude (blue). Middle: Time evolution of density imbalance (red) between corners and bulk, and subsystem magnetization (blue). Bottom: Normalized entanglement entropy evolution. All results are averaged over 10 noise realizations; shaded areas indicate standard deviation across realizations. Data were obtained using ED.

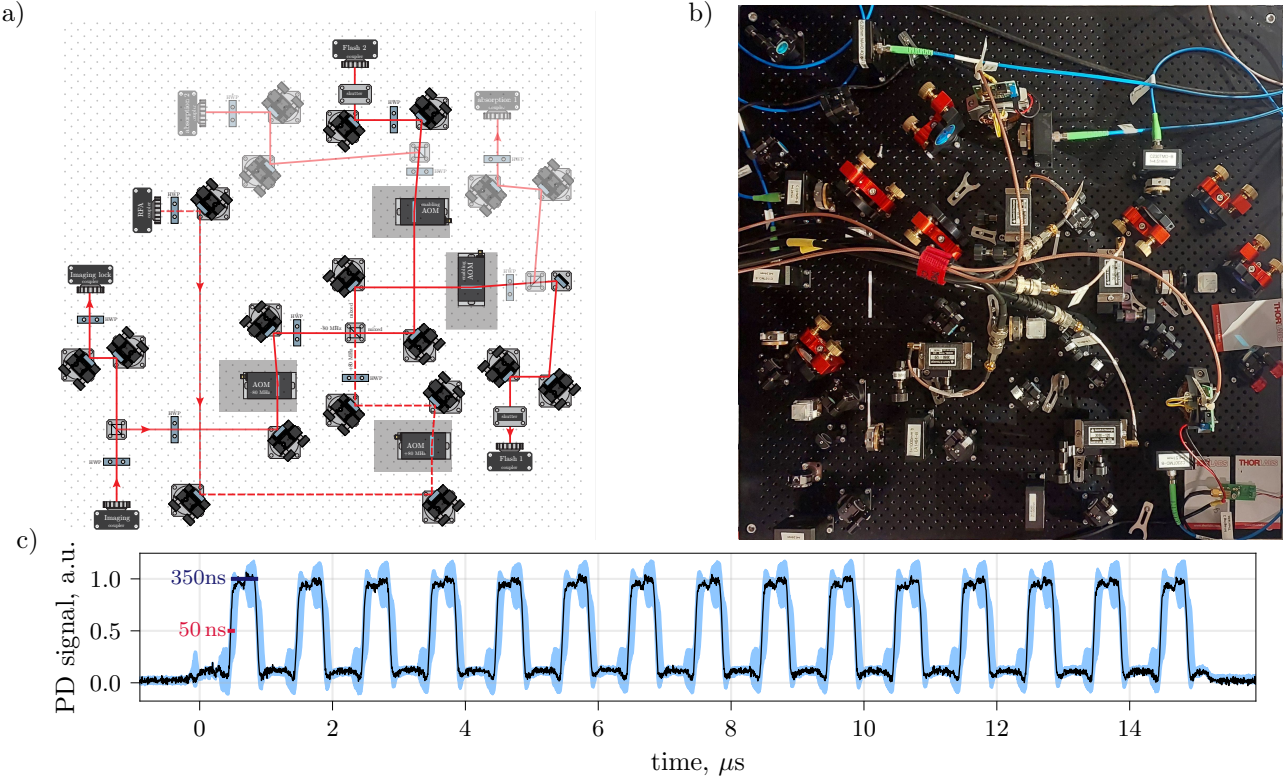


Figure 14: **Distribution board for flashing.** a) Optical layout of the board used to combine and control light for free-space imaging states $|3\rangle$ and $|6\rangle$. b) Experimental implementation. c) PD signal of the flashing measured on an oscilloscope (black – a single experimental run, blue – the standard deviation over 20 runs, red – rise time).

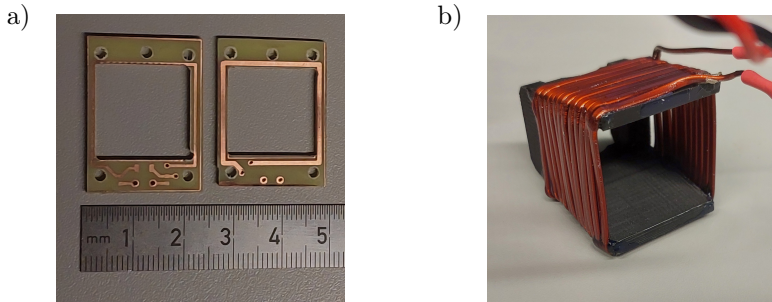


Figure 15: **RF and MW antennas used for spin control.** (a) PCB-based radiofrequency (RF) antenna used for driving spin transitions at MHz frequencies. (b) Microwave (MW) loop antenna, designed to efficiently couple to hyperfine transitions in ${}^6\text{Li}$. These antennas are used for coherent spin manipulation.

1 Introduction

1.1 Quantum Simulation with Fermionic Tweezer Arrays

The simulation of strongly correlated quantum systems remains one of the central challenges in modern physics. While exact numerical methods have provided deep insights in one-dimensional settings, the computational cost of simulating many-body dynamics in higher dimensions grows exponentially with system size, rendering classical approaches impractical. As first envisioned by Feynman, this motivates the development of physical quantum simulators that emulate target Hamiltonians using intrinsically quantum mechanical systems. Among several available platforms, ultracold atoms in optical potentials offer an exceptionally clean and versatile environment for realizing a broad range of many-body models, including the Fermi-Hubbard model relevant for high-temperature superconductivity [5, 7].

In particular, fermionic atoms loaded into optical lattices have enabled the realization of the two-dimensional Fermi-Hubbard model, with site-resolved imaging revealing spin correlations and signatures of antiferromagnetic ordering [11, 1]. These advances highlight the power of quantum gas microscopy in exploring equilibrium properties of lattice fermions. However, conventional approaches rely on thermal loading of large ensembles into periodic potentials, which often results in uncontrolled entropy and random filling defects. As a consequence, the system is typically initialized in a thermal ensemble, and the preparation of arbitrary low-entropy many-body states remains difficult.

Optical tweezer arrays offer an alternative, bottom-up approach. By providing single-site control, they allow deterministic preparation of initial states, flexible geometries, and site-selective addressing. While initially developed in the context of Rydberg atom arrays [2], these platforms have recently been extended to degenerate fermions, enabling programmable few-body Fermi-Hubbard dynamics [13, 14]. Such results position tweezer arrays as a promising architecture for scalable fermionic quantum simulators.

This thesis contributes to the development of a quantum simulation platform based on ultracold fermionic ${}^6\text{Li}$ atoms in a two-dimensional optical tweezer array. In this approach, the array is used for high-fidelity state preparation and control, while the optical lattice serves as the environment for Hamiltonian evolution. Compared to direct loading into a lattice, this separation of initialization and dynamics enables more efficient cooling, deterministic control over occupation patterns, and reduced cycle times. To support this workflow, we develop methods for spin-resolved free-space imaging, arbitrary pattern initialization via spin-selective spilling, and precise tweezer depth balancing.

Looking ahead, such a platform opens the door to nonequilibrium quantum dynamics. For instance, by performing randomized local operations followed by spin-resolved measurements, one can access entanglement entropy via measurement statistics [3]. These protocols offer a practical way to characterize entanglement growth and scrambling, even in regimes where full state tomography is infeasible. Extending such techniques to fermionic systems will provide new insights into thermalization, localization, and quantum information dynamics in strongly correlated matter.

In summary, this work supports the realization of a bottom-up fermionic quantum simulator by combining deterministic state preparation with single-atom, spin-resolved readout. These tools provide a foundation for studying both static and dynamical aspects of the Fermi-Hubbard model in a highly controlled setting.

1.2 Thesis Outline

This thesis describes the development of experimental and computational tools for the preparation and probing of fermionic many-body states in a programmable optical tweezer array. The overarching goal is to enable bottom-up quantum simulation of lattice models, with precise control over initial conditions and single-atom, spin-resolved readout.

Sec. 2 presents the implementation of spin-resolved single-atom imaging of ${}^6\text{Li}$ in free space. The section describes the optical layout, the image processing pipeline, and introduces the Su-Schrieffer-Heeger model as a conceptual framework for understanding spin-dependent imaging dynamics.

Sec. 3 focuses on the creation and control of two-dimensional tweezer arrays. The section begins with the optical setup and AOD control, followed by a detailed discussion of calibration procedures and tweezer depth balancing using both camera-based and atom-based feedback. A key result is the development of a spin-selective spilling technique, enabling the preparation of spin- and site-resolved occupation patterns. Arbitrary configurations are realized through iterative removal steps, formalized via boolean matrix factorization.

Sec. 4 introduces the concept of a matter-wave magnifier—a lensing scheme designed to enhance spatial resolution for future lattice imaging. Although not yet implemented experimentally, fast simulations of wavefunction propagation and Monte Carlo sampling are presented to validate the scheme.

Finally, Sec. 5 outlines numerical approaches for simulating Fermi-Hubbard dynamics on small lattices. The computational framework combines exact diagonalization and Krylov-based time evolution, accelerated on GPU hardware. These tools enable simulations of dynamics in the presence of noise and disorder, and serve as a theoretical reference for upcoming experimental investigations.

2 Single-atom spin-resolved free-space imaging

2.1 Motivation and background

...

2.2 Experimental setup

...

2.3 Image processing

...

2.4 Spin-resolved detection

...

3 Tweezer array system

3.1 Motivation and concept

Optical tweezer arrays provide a flexible platform for preparing ultracold atomic systems with site-resolved control. By trapping individual atoms in focused laser beams, it becomes possible to initialize many-body states with controlled geometry, low entropy, and tunable local parameters.

In our setup, a two-dimensional array of tweezers is created using two orthogonal acousto-optic deflectors (AODs). Each AOD diffracts multiple beams along one axis, and their intersection forms the full array. The resulting intensity at site (i, j) factorizes as $P_{ij} = H_i V_j$, where H_i and V_j are set by the drive amplitudes applied to each AOD. This structure simplifies calibration and allows fast control of the entire array using a small number of parameters.

Compared to holographic or lattice-based approaches, the AOD system offers rapid reconfigurability and independent control of individual traps. This enables preparation of custom spin and density patterns, as well as dynamic manipulation during the experimental sequence. Such capabilities are useful, for example, for initializing specific configurations, removing defects, or performing spatially selective operations before loading atoms into an optical lattice for further evolution.

AOD operation. Each AOD consists of a crystal driven by a piezoelectric transducer. An incoming laser beam $(\mathbf{k}_{\text{in}}, \omega_{\text{in}})$ interacts with the induced acoustic wave (\mathbf{q}, Ω) via Bragg diffraction, producing an outgoing beam $(\mathbf{k}_{\text{out}}, \omega_{\text{out}})$:

$$\mathbf{k}_{\text{out}} = \mathbf{k}_{\text{in}} + \mathbf{q}, \quad \omega_{\text{out}} = \omega_{\text{in}} + \Omega.$$

The frequency Ω determines the deflection angle θ through the Bragg condition, while the amplitude of the RF signal controls the diffracted optical power. Each RF tone can be described by a triple $(\Omega_j, a_j, \varphi_j)$, corresponding to its frequency, amplitude, and phase. Applying a set of such tones to an AOD results in a superposition of multiple diffracted beams, with the amplitude a_j determining the power in each beam and the phase φ_j influencing their relative coherence.

Factorized intensity distribution. To create 2D arrays, we combine two AODs oriented along orthogonal axes (fig. 5a), as described in [4]. Each axis is driven by a set of RF tones. In the paraxial approximation, the resulting 2D intensity pattern can be written as a rank-1 product of two vectors:

$$P_{ij} = H_i V_j,$$

where H_i and V_j correspond to the powers of individual beams generated by the horizontal and vertical AOD, respectively. The factorization of the output power can be verified via:

$$P \stackrel{\text{SVD}}{=} \sum_r \Lambda_r \mathbf{H}_r \mathbf{V}_r^T, \quad \text{factorisability} = \Lambda_0 / \sum_r \Lambda_r \quad (1)$$

which provides a natural measure of factorization. For arrays ranging from 2×2 to 10×10 , the factorisability measure $\Lambda_0 / \sum_r \Lambda_r$ is consistently above 0.99. For the 4×4 array used in most of our experiments, we obtain a typical value of 0.997(1).

Tweezer array control. The tweezer output beam powers are nonlinear functions of the input amplitudes \mathbf{a} :

$$P_j = F_j(\mathbf{a}) = \cancel{F_j(\mathbf{0})} + F'_{ji} a_i + \frac{1}{2} F''_{j i_1 i_2} a_{i_1} a_{i_2} + \dots \quad (2)$$

The goal is to control¹ the full matrix P_{ij} using only two sets of parameters: horizontal amplitudes \mathbf{h} and vertical amplitudes \mathbf{v} .

It will later be necessary to reconstruct (H_i, V_j) from measured intensity distribution P_{ij} , so it is convenient to choose a factorized model $P_{ij} = \Lambda H_i V_j$, with the normalization:

$$\sum_i H_i = \sum_j V_j = 1, \quad \sum_{ij} P_{ij} = \Lambda.$$

This allows for an explicit decomposition:

$$\frac{1}{\Lambda} \sum_j P_{ij} = H_i \sum_j V_j = H_i, \quad \frac{1}{\Lambda} \sum_i P_{ij} = V_j \sum_i H_i = V_j, \quad \sum_{ij} P_{ij} = \Lambda, \quad (3)$$

which is fully equivalent to a rank-1 SVD of P_{ij} .

It is worth noting that, as shown in Fig. 5d, the total scale parameter Λ defined in this way is proportional to the total input amplitude, $a_{\text{sum}} = \sum_j h_j + \sum_j v_j$. This effectively decouples local balancing from global power constraints, simplifying the control problem.

¹For amplitudes in the range $a_i \in [0.7, 1.0]$, we find that a linear or quadratic approximation suffices. In practice, we reconstruct the Jacobian matrix F'_{ji} using camera-based calibration, as discussed in Sec. 3.4.

3.2 Optical setup

Beam collimation and polarization. The tweezer array is formed by delivering light from a fiber outcoupler and collimating it with an $f = 40$ mm achromatic lens mounted on a translation stage for precise control. To ensure efficient diffraction through the acousto-optic deflectors (AODs), horizontal polarization is set using a $\lambda/2$ waveplate and a polarizing beam splitter (PBS). Correct alignment of the PBS is verified by tracking the beam position on a camera before and after insertion.

Acousto-optic deflectors and relay imaging. The array is generated using a pair of orthogonally mounted AODs, each mounted on custom blocks to maintain a common beam height of 100 mm. The beam is guided into the first AOD using two mirrors, and its alignment is optimized to maximize both transmission and diffraction efficiency (typically exceeding 90% at 65 MHz). The two AODs are connected via a 4f relay built from achromatic lenses in a 30 mm cage system. Precise positioning is achieved by aligning the relay externally using collimated light and checking for minimal wavefront distortion on a shear plate. An iris at the Fourier plane of the relay filters out the zeroth diffraction order.

Telescope and beam expansion. After the second AOD, the beam is expanded using a telescope consisting of $f = 150$ mm and $f = 500$ mm lenses. The alignment ensures that the beam is collimated and centered on both lenses. The position of the second lens is mechanically fixed, while the telescope length is adjusted via mirror positions to achieve good collimation, verified with a shear plate. The zeroth-order beam after the second AOD is blocked at the intermediate focus.

Monitoring and power balancing. A flip mirror is installed in the beam path to optionally redirect the light into a monitoring camera without disturbing the main optical alignment. This enables fast access to the tweezer array profile during alignment or balancing procedures.

We avoid using a back-side polished mirror for beam sampling in front of the camera. Although commonly employed for its simplicity, such mirrors introduce ([? add measured data: october 2024](#)) spatially varying interference fringes due to reflections from different internal surfaces of the substrate. These fringes distort the measured intensity distribution, especially for rays entering the camera at different angles and positions. This effect becomes critical when calibrating the response of the AODs, as it leads to systematic errors in measured beam uniformity. Instead, we sample the beam with a removable flip mirror that fully redirects the beam, ensuring an undistorted and angle-independent intensity profile at the camera plane.

3.3 State preparation

Tweezer loading. We begin by preparing a spin-balanced mixture in the two lowest hyperfine states, $|1\rangle$ and $|2\rangle$, using a compressed magneto-optical trap (MOT). The atoms are initially loaded into a crossed ODT, where we perform evaporative cooling. This follows closely the sequence described in [4].

After cooling, the atoms are transferred into a tightly focused optical tweezer potential. The loading process relies on the so-called *dimple trick* [15], where a tightly confined but deep tweezer potential is superimposed onto the wider ODT reservoir. Because the tweezer affects only a small region of the total cloud, the global temperature T remains approximately unchanged, while the local chemical potential is enhanced. In this regime, the average occupation number $\bar{n}(E_i)$ of a single-particle state i with energy E_i follows the Fermi-Dirac distribution:

$$\bar{n}(E_i) = \frac{1}{e^{(E_i - \mu)/k_B T} + 1}. \quad (4)$$

If the energy gap between the ground state E_0 and the Fermi energy E_F is increased such that $(E_0 - E_F)/k_B \gg T$, then $\bar{n}(E_0) \rightarrow 1$. This ensures near-unity occupation of the lowest level, which provides an ideal starting point for deterministic preparation. In our experiment, this condition is achieved by ramping on the tweezer adiabatically while continuing evaporation inside the tweezer. The full loading and cooling sequence is depicted in Fig. 9.

Deterministic few-body preparation via spilling. To isolate a well-defined number of atoms in the lowest motional states of the tweezer, we use the *spilling technique*, as described in [15, 9]. This method relies on tilting the potential with a magnetic field gradient and reducing the trap depth to allow atoms above a threshold energy to tunnel out. The resulting states are shown in Fig. 7. [See Appendix for details.](#)

The spilling sequence is performed at a magnetic field of 527 G, where the two spin states are nearly non-interacting. A magnetic field gradient of 20 G/cm creates a linear tilt, and the tweezer power is lowered to a value that sets the spill threshold. After a short tunneling time, the trap depth is ramped back up to recapture the remaining atoms. By empirically optimizing these parameters, we achieve deterministic preparation of two atoms per tweezer with a fidelity of approximately 95 %. This sequence results in high-fidelity preparation within a total experimental cycle time of less than 2 s.

Стоит сказать, что система достаточно симметрична по отношению к уменьшению tweezer depth во время spilling или увеличению градиента.

3.4 Control

Frequency to position mapping. To extract the local intensities P_{ij} from camera images, we need to determine which pixels correspond to which tweezer sites. For this purpose, we define an affine transformation from the drive frequency space $(\omega_{\text{hor}}, \omega_{\text{ver}})$ to image plane coordinates (x, y) :

$$\mathbf{r} = H\boldsymbol{\omega}, \quad \Leftrightarrow \quad \begin{pmatrix} x \\ y \end{pmatrix} = \begin{pmatrix} h_{11} & h_{12} & h_{13} \\ h_{21} & h_{22} & h_{23} \end{pmatrix} \begin{pmatrix} \omega_{\text{hor}} \\ \omega_{\text{ver}} \\ 1 \end{pmatrix}.$$

Here, H is a 2×3 matrix calibrated from a set of measured spot positions. For example, one can measure \mathbf{r}_j for random frequency vectors $\boldsymbol{\omega}_j \in [\omega_{\min}, \omega_{\max}]$, construct the matrices ω_{ij} with $i \in \{\text{hor}, \text{ver}\}$ and r_{ij} with $i \in \{x, y\}$, and solve the least-squares problem:

$$r = H\boldsymbol{\omega}, \quad \Rightarrow \quad r\boldsymbol{\omega}^T = H\boldsymbol{\omega}\boldsymbol{\omega}^T \quad \Rightarrow \quad r\boldsymbol{\omega}^T (\boldsymbol{\omega}\boldsymbol{\omega}^T)^{-1} = H. \quad (5)$$

This transformation defines a region of interest around each tweezer, within which we compute the integrated pixel intensity after background subtraction. The resulting values are proportional to the optical powers P_{ij} .

Linear reconstruction. The mapping from input amplitudes \mathbf{a} to optical power is approximated by Eq. (2). In the regime $a_i \in [0.85, 0.95]$, a linear approximation is sufficient². We construct the Jacobian matrix F'_{ji} by fitting a linear regression model to a dataset of amplitude–intensity pairs. The resulting crosstalk matrix is shown in Fig. 5b. It is approximately diagonal, with comparable diagonal entries and off-diagonal elements typically reaching up to 30% in magnitude relative to the diagonal, due to power redistribution between neighboring tones. Crosstalk between the horizontal and vertical AODs remains negligible.

The quality of the linear fit for the 4×4 array is illustrated in Fig. 5e. The total intensity (Fig. 5d) scales linearly with the average input amplitude, yielding $R^2 > 0.99$. Relative residuals are normally distributed with width 0.3%, confirming the applicability of the model in this range.

Power-aware optimization. In the presence of limited laser power and finite AOM diffraction efficiency, we prefer solutions where all amplitudes remain close to 1. This preference can be incorporated into the optimization objective. In addition to minimizing intensity imbalance, we penalize deviations of the average amplitudes from a target value (e.g., 0.9).

3.5 Tweezer depth balancing

Можно использовать и калибровку отдельно для каждого AOD, не задумываясь тогда про SVD. В рамках этой работы такой подход не тестировался. Хочется подчеркнуть, что подход с SVD гарантировано работает и для double AOD [ссылка], где crosstalk между двумя направлениями может быть сильнее.

Precise control over the depth of each optical tweezer is essential for preparing few-fermion systems via spilling techniques. In our setup, each tweezer is initially loaded with approximately 100 atoms, which are then selectively removed by ramping down the potential depth. The number of remaining atoms as a function of spill power x_{sp} exhibits a quantized staircase structure, reflecting the discrete energy levels of the 1D harmonic oscillator. This behavior can be characterized by a step plot [9].

Step plot. To characterize this behavior in our tweezer array, we measure step plots for all sites simultaneously. Figure 6a shows the result for a 4×4 array. For each value of x_{sp} , we acquire 70 experimental realizations and compute the average photon signal per site. This signal serves as a robust proxy for atom number. In contrast to single-atom counting, this approach is parameter-free and effective even for large initial occupancies.

Uniformity characterization. To quantify depth inhomogeneity across the array, we fit each step trace with a sigmoid function:

$$\text{sigmoid}(x) = \frac{A_j}{1 + \exp(-(x - x_j)/\sigma_j)},$$

where x_j denotes the center of the step and σ_j its width for tweezer j . We define a relative uniformity metric as $\text{std}(x_j)/\langle x_j \rangle$. After camera-based balancing (Sec. 3.4), this metric typically yields $\sim 3\%$, which is insufficient for deterministic preparation across the array. A more precise balancing procedure is therefore required.

Single-value feedback. To further improve uniformity, we apply an iterative atom-based feedback scheme. Rather than fitting full step plots, we operate at a single point on the slope of the transition, near the half-filling level $A_j/2$. At this point, the sigmoid can be approximated by a linear response:

$$\text{sigmoid}(x) \approx \frac{A_j}{4\sigma_j}x - \frac{A_j x_j}{4\sigma_j},$$

²For wider amplitude ranges, higher-order terms can be added to the model. However, this is unnecessary in the present context.

assuming $x_j \gg \sigma_j$. In the feedback loop, we do not use the fitted sigmoid parameters directly. Instead, we measure a single photon-count matrix M_{ij} and treat it as a linear proxy for the power matrix P_{ij} . Since the sigmoid offset shift = $A_j x_j / (4\sigma_j)$ is known from the fits, we approximate:

$$M_{ij} + \text{shift} \propto P_{ij} = \Lambda H_i V_j. \quad (6)$$

We then factorize this matrix using the method introduced in (3) and update the amplitudes according to:

$$h \rightarrow h + \gamma(H - H_0), \quad v \rightarrow v + \gamma(V - V_0),$$

where (H_0, V_0) is the target point, and γ is the feedback rate. This model-free procedure avoids full sigmoid fitting and operates directly on experimental measurements.

Figure 6b shows the result of applying this single-value feedback (SVF) protocol to a 4×4 array. After five iterations, the relative deviation of the fitted step centers is reduced to 0.7(2)%, well within the plateau width (typically $\pm 5\%$), enabling deterministic state preparation across the full array. [Add fig. with single value feedback progress.](#)

На Fig. 8а представлен процесс of применяя SVF протокол к 6×6 массиву. Коэффициент пропорциональности в (6) равен $A/4\sigma \sim 10(1)$ (для графика выбрано среднее значение) для нашего эксперимента.

3.6 Spin-selective spilling

After balancing the tweezer depths and performing standard spilling to prepare unit filling (one atom in state $|1\rangle$ and one in $|2\rangle$ per site), atoms in a selected spin state can be selectively removed while leaving the other unaffected. This enables the preparation of arbitrary spin-resolved configurations, a crucial ingredient for bottom-up simulation of spinful many-body systems.

Magnetic-field dependence. The key idea relies on the difference in magnetic moments between the hyperfine ground states. As shown in Fig. 3b, the energy of state $|2\rangle$ exhibits a maximum near 27 G, where its magnetic moment vanishes: $\mu_{|2\rangle} = \partial E / \partial B = 0$. In contrast, state $|1\rangle$ has a sizable negative magnetic moment at this field ([write down value](#)). As a result, when a magnetic field gradient is applied at $B = 27$ G, only atoms in state $|1\rangle$ experience a significant force and are spilled from the traps.

Spin-selective removal. The experiment starts with a $|1\rangle-|2\rangle$ spin mixture at unit filling in each tweezer. The magnetic field is ramped to 27 G, and a field gradient is applied. This results in spin-selective spilling: atoms in state $|1\rangle$ are removed, while those in $|2\rangle$ remain confined.

The crossed AOD configuration enables control over the local optical power P_{ij} through factorized amplitudes, such that $P_{ij} = H_i V_j$. This allows us to define arbitrary rank-1 intensity masks and thus selectively apply spilling to specific subsets of sites.

This protocol enables single-shot removal of state $|1\rangle$ atoms without perturbing state $|2\rangle$, providing a flexible method for initializing spin-imbalanced or spatially patterned states. The performance of the method in terms of selectivity and overall fidelity is summarized in [Fig. ?](#). Sequential applications of such steps to prepare arbitrary configurations are discussed in Sec. 3.7.

3.7 Arbitrary occupation loading

The ability to prepare arbitrary atom configurations is a key ingredient for bottom-up quantum simulation. After obtaining unit filling for both spin states (as discussed in Sec. 3.5 and 3.6), we implement a multi-stage spilling sequence that enables spin- and site-resolved initialization of arbitrary patterns.

The loading sequence proceeds in several steps:

1. Prepare a $|1\rangle-|2\rangle$ spin mixture with unit filling across the tweezer array.
2. Perform global spilling steps to remove atoms from factorized intensity patterns P_{ij} , affecting both spin states.
3. Apply spin-selective spilling steps to remove atoms in state $|1\rangle$ from additional factorized subsets of sites.
4. Flip the remaining atoms $|1\rangle \leftrightarrow |2\rangle$ using a microwave π -pulse.
5. Repeat spin-selective spilling to further refine the configuration

Factorized removal. Each spilling step removes atoms from sites where the local tweezer depth P_{ij} falls below a certain threshold. Since we can impose any rank-1 intensity mask $P_{ij} = H_i V_j$, it is possible to tailor the removal region to arbitrary product forms. To remove a single atom at site (i', j') , for example, we reduce $H_{i'}$ and $V_{j'}$ by a factor $\eta < 1$ and simultaneously increase the global power by η . This yields a relative intensity of $1/\eta$ at the intersection, while leaving all other sites unchanged or increased in depth. In this way, we can reliably isolate and remove atoms from any desired factorized subset.

Boolean decomposition. We represent the cumulative removal pattern as a binary matrix W_{ij} , where $W_{ij} = 1$ indicates that the atom at site (i, j) has been removed. Each spilling operation adds a binary outer product $u_i^\lambda v_j^\lambda$ via

Boolean logic ($1 + 1 = 1$). An arbitrary target pattern can therefore be reached through a sequence of such operations:

$$W_{ij} = \bigvee_{\lambda=1}^r u_i^\lambda v_j^\lambda, \quad (7)$$

which defines the exact Boolean matrix factorization (EBMF) of the removal matrix. In the worst case, any binary $n \times n$ matrix admits such a decomposition using at most n steps.

Optimal EBMF. While a naive strategy—such as row- or column-wise removal—may require up to n iterations, we find that optimal EBMF often reduces this number. The problem of finding an exact Boolean matrix factorization with minimal rank is known to be NP-complete [10] and NP-hard to approximate [8]. Nevertheless, for arrays up to 10×10 , optimal decompositions can be computed in a few seconds using a SAT solver. These improvements are particularly useful for minimizing experimental cycle time and improving overall sequence fidelity. A full discussion of the EBMF algorithm and its implementation is presented in Appendix.

4 Matter-wave magnifier

4.1 Motivation and overview

...

4.2 Numerical modeling

...

5 Fermi-Hubbard model: numerical approaches and simulations

5.1 Motivation and experimental relevance

...

5.2 Theoretical and numerical methods

...

5.3 GPU-accelerated implementation

...

5.4 Simulations of noisy dynamics

...

6 Appendix

6.1 Boolean matrix factorization

...

References

- [1] Martin Boll, Timon A. Hilker, Guillaume Salomon, Ahmed Omran, Jacopo Nespolo, Lode Pollet, Immanuel Bloch, and Christian Gross. Spin- and density-resolved microscopy of antiferromagnetic correlations in Fermi-Hubbard chains. *Science*, 353(6305):1257–1260, September 2016.
- [2] Antoine Browaeys and Thierry Lahaye. Many-body physics with individually controlled Rydberg atoms. *Nat. Phys.*, 16(2):132–142, February 2020.
- [3] Tiff Brydges, Andreas Elben, Petar Jurcevic, Benoît Vermersch, Christine Maier, Ben P. Lanyon, Peter Zoller, Rainer Blatt, and Christian F. Roos. Probing Rényi entanglement entropy via randomized measurements. *Science*, 364(6437):260–263, April 2019.
- [4] Marcus Culemann. Construction and Control of a Dark Spot Optical Tweezer Array for a Quantum Gas Microscope. Master’s thesis, 2024.
- [5] Tilman Esslinger. Fermi-Hubbard Physics with Atoms in an Optical Lattice. *Annual Review of Condensed Matter Physics*, 1(Volume 1, 2010):129–152, August 2010.
- [6] Michael Eric Gehm. *Preparation of an optically-trapped degenerate Fermi gas of 6Li: Finding the route to degeneracy*. PhD thesis, January 2003.
- [7] Christian Gross and Immanuel Bloch. Quantum simulations with ultracold atoms in optical lattices. *Science*, 357(6355):995–1001, September 2017.
- [8] Hermann Gruber and Markus Holzer. Inapproximability of Nondeterministic State and Transition Complexity Assuming $P \neq NP$. In *Developments in Language Theory*, pages 205–216, Berlin, Heidelberg, 2007. Springer.
- [9] Marvin Holten. *From Pauli Blocking to Cooper Pairs: Emergence in a Mesoscopic 2D Fermi Gas*. PhD thesis, 2022.
- [10] James Orlin. Contentment in graph theory: Covering graphs with cliques. *Indagationes Mathematicae (Proceedings)*, 80(5):406–424, January 1977.
- [11] Maxwell F. Parsons, Anton Mazurenko, Christie S. Chiu, Geoffrey Ji, Daniel Greif, and Markus Greiner. Site-resolved measurement of the spin-correlation function in the Fermi-Hubbard model. *Science*, 353(6305):1253–1256, September 2016.
- [12] Friedhelm Serwane. *Deterministic preparation of a tunable few-fermion system*. Dissertation, 2011.
- [13] Benjamin M. Spar, Elmer Guardado-Sánchez, Sungjae Chi, Zoe Z. Yan, and Waseem S. Bakr. Realization of a Fermi-Hubbard Optical Tweezer Array. *Phys. Rev. Lett.*, 128(22):223202, June 2022.
- [14] Zoe Z. Yan, Benjamin M. Spar, Max L. Prichard, Sungjae Chi, Hao-Tian Wei, Eduardo Ibarra-García-Padilla, Kaden R.A. Hazzard, and Waseem S. Bakr. Two-Dimensional Programmable Tweezer Arrays of Fermions. *Phys. Rev. Lett.*, 129(12):123201, September 2022.
- [15] Gerhard Zürn. *Few-fermion systems in one dimension*. PhD thesis, 2012.
- [16] N. Šibalić, J. D. Pritchard, C. S. Adams, and K. J. Weatherill. ARC: An open-source library for calculating properties of alkali Rydberg atoms. *Computer Physics Communications*, 220:319–331, November 2017.